ADVANCING EARTH AND SPACE SCIENCE

Geophysical Research Letters

RESEARCH LETTER
10.1029/2021GL096972

Possible Anthropogenic Enhancement of Precipitation in the Sahel-Sudan Savanna by Remote Agricultural Irrigation

Yujin Zeng[1], P. C. D. Milly[2], Elena Shevliakova[3], Sergey Malyshev[3], M. H. J. van Huijgevoort[1,4], and K. A. Dunne[5]

[1]Program in Atmospheric and Oceanic Sciences, Princeton University, Princeton, NJ, USA, [2]U.S. Geological Survey, Princeton, NJ, USA, [3]Geophysical Fluid Dynamics Laboratory, National Oceanic and Atmospheric Administration, Princeton, NJ, USA, [4]KWR Water Research Institute, Nieuwegein, The Netherlands, [5]U.S. Geological Survey, Cornish, NH, USA

Key Points:

- Irrigation in the Middle East and South Asia may considerably enhance rainfall in the Sahel-Sudan Savanna (SSS)
- The enhancement of precipitation arises through a reduction in the gradient of moist static energy from the Sahara to the tropics
- The risk and severity of drought in the SSS may be reduced by remote irrigation

Supporting Information:

Supporting Information may be found in the online version of this article.

Correspondence to:

Y. Zeng,
yujinz@princeton.edu

Citation:

Zeng, Y., Milly, P. C. D., Shevliakova, E., Malyshev, S., van Huijgevoort, M. H. J., & Dunne, K. A. (2022). Possible anthropogenic enhancement of precipitation in the Sahel-Sudan Savanna by remote agricultural irrigation. *Geophysical Research Letters*, *49*, e2021GL096972. https://doi.org/10.1029/2021GL096972

Received 9 NOV 2021
Accepted 5 MAR 2022

Abstract

The local climatic impacts of historical expansion of irrigation are substantial, but the distant impacts are poorly understood, and their governing mechanisms generally have not been rigorously analyzed. Our experiments with an earth-system model suggest that irrigation in the Middle East and South Asia may enhance rainfall in a large portion of the Sahel-Sudan Savanna (SSS) to an extent comparable and opposite to its suppression by other anthropogenic climate drivers during the last several decades. The enhancement arises through a reduction in the meridional gradient of moist static energy from the Sahara Desert to the tropical rainforests. An implication of this study is that remote irrigation is a possible factor affecting the risk of drought and famine and, thus, future water security in the SSS region.

Plain Language Summary

The impacts of historical expansion of agricultural irrigation on local precipitation are robust and profound, but whether irrigation can change precipitation in remote areas is poorly understood, and governing mechanisms responsible for the remote links generally have not been rigorously analyzed. Our numerical experiments with an earth-system model suggest that irrigation in the Middle East and South Asia may enhance rainfall in a large portion of the Sahel-Sudan Savanna (SSS). The magnitude of the enhancement is comparable to the suppression of precipitation induced by other anthropogenic climate drivers such as greenhouse emissions. The enhancement arises through a change in the large-scale patterns of atmospheric moisture and temperature from the Sahara Desert to the tropical rainforests. Growth of remote irrigation should be considered as a possible factor affecting the risk of drought and famine in the SSS such as that experienced in the 1970s–1980s. Future regional water security in the SSS could be affected by distant water management-groundwater depletion in South Asia and the pace of rehabilitation of war-damaged irrigation infrastructure in the Tigris-Euphrates valley.

1. Introduction

In numerical experiments with global climate models, some common hydrologic responses to irrigation have been noted. These include enhancement of precipitation over and/or in the downwind vicinity of the irrigated regions (B. I. Cook et al., 2015; de Vrese et al., 2016; Guimberteau et al., 2013; Puma & Cook, 2010; Thiery et al., 2017; Wei et al., 2013; Zeng et al., 2017) and reduction in precipitation associated with the South Asian Monsoon (B. I. Cook et al., 2015; Guimberteau et al., 2013; Puma & Cook, 2010; Zeng et al., 2017). Possible remote (i.e., >2,000 km distant) responses, which show virtually no consistency across models, include reduction of precipitation in the Amazon River basin and Australia (Thiery et al., 2017) and increase of precipitation in some other semiarid regions (de Vrese et al., 2016; Puma & Cook, 2010; Thiery et al., 2017; Zeng et al., 2017), including, in some cases, the semi-arid region between the Sahara Desert and the tropical rainforests to its south. Together with this divergence of findings, the general absence of analyses of mechanisms controlling the reported remote responses calls into question their plausibility and robustness.

In our analysis of the remote responses of the complex climate system to irrigation, we have found that the moist static energy (MSE) budget provides a useful framework. The MSE budget is closely related to convective variability and precipitation anomalies in the tropics (Inoue & Back, 2015; Masunaga, 2012; Raymond, 2000). Consequently, it has been useful for understanding tropical precipitation response to external forcings (Back & Bretherton, 2006; Hill et al., 2017, 2018; Jalihal et al., 2020).

To examine the precipitation response to global irrigation and analyze the controlling mechanisms, we conducted numerical experiments using the Geophysical Fluid Dynamics Laboratory earth-system model ESM2Mb (Dunne et al., 2012, 2013; Malyshev et al., 2015) with an added irrigation module, and we analyzed the MSE budget to explain the model's strong remote response of SSS precipitation to global irrigation.

2. Methods

2.1. Modification of Land Component of ESM2Mb for Irrigation

ESM2Mb is a coupled atmosphere-ocean general circulation model combined with a global carbon cycle model and having atmospheric and land horizontal resolution of 2° latitude by 2.5° longitude. To implement irrigation in the land component LM3 (Milly et al., 2014) of ESM2Mb, we prescribed, for each model grid cell, the estimated time-dependent historical area within that cell equipped for irrigation. On those areas, we supplied irrigation water, interactively, and only if needed, in an amount sufficient to minimize plant water stress. The representation of time-varying irrigated area in LM3 is facilitated by its dynamic sub-grid tiling structure. In LM3, each grid cell is divided into a mosaic of independent tiles. Each tile is defined on a substrate of either soil, lake, or glacier. Any lake or glacier is permanently represented by a single tile, but the number of soil tiles, which contain vegetation, can vary in space and time. LM3 simulates vegetation dynamics, including vegetation growth, its interaction with the atmosphere and underlying soil column, and disturbances such as fire, natural mortality and human land use. A tile can contain one of five different vegetation types (C3 or C4 grass; or temperate, tropical broadleaf, or cold-evergreen trees); these evolve dynamically according to biomass amount and biogeographical rules (Dunne et al., 2012; Milly et al., 2014; Shevliakova et al., 2009). Areas with different histories of land use management (i.e., primary, pasture, crop, and secondary) occupy different tiles. Rain-fed and irrigation-equipped crops (all treated as crops) are given separate tiles.

On tiles equipped for irrigation, it is assumed here that plant water requirements are fully satisfied by irrigation. The irrigation rate is made proportional to the difference between the transpiration demand and a soil-water supply function according to

$$I = k(T_0 - W) \tag{1}$$

where I (kg m^{-2} s^{-1}) is the irrigation rate; T_0 (kg m^{-2} s^{-1}) is the transpiration demand, which is the hypothetical transpiration rate when soil-water supply is not limiting; W (kg m^{-2} s^{-1}) is the maximum rate at which the soil can deliver water to the root system of the vegetation; and k (dimensionless) is a location-dependent irrigation factor that is used to maximize the crop transpiration with a minimal water requirement; k is pre-determined by sensitivity experiments. Values of k are greater than 1, because irrigation water is consumed not only by enhancement of transpiration, but also by enhancement of evaporation from interception storage and the soil surface and by enhancement of runoff. Irrigation water is added to the precipitation delivered by the model to the top of the crop canopy.

Water used for irrigation is provided as much as possible by rivers and lakes in the grid cell that contains the irrigated tile. If necessary, surface water is also provided by adjacent grid cells. Any additional water requirement is provided by groundwater—first from available groundwater in the irrigated tile, and then, if necessary, from deep groundwater, which is below the domain of the model. Text S1 in Supporting Information S1 gives more information about the irrigation module.

2.2. Moist Static Energy Budget Analysis

MSE, denoted symbolically here by h (J kg^{-1}), is a sum of sensible and latent heat contents and gravitational potential energy of air,

$$h = c_p T + gz + L_v q_v - L_f q_i \tag{2}$$

where c_p (J kg^{-1} K^{-1}) is the specific heat of air at constant pressure, T (K) is temperature, g (m s^{-2}) is the gravitational constant, z (m) is geopotential height, L_v (J kg^{-1}) is the latent heat of vaporization of water, q_v (kg kg^{-1}) is specific humidity, L_f (J kg^{-1}) is the latent heat of fusion of water, and q_i (kg kg^{-1}) is specific mass of ice. The principle of energy conservation implies a balance among column-integrated storage of MSE, horizontal and vertical advection, and radiative heating (Text S4 in Supporting Information S1). This balance facilitates the interpretation of how an externally imposed change in one term (in our case, the horizontal advection) drives changes in the other terms.

2.3. Experimental Design

Two ensembles of ESM2Mb simulations, each with eight experiments, were conducted for the period 1902–2015. In the irrigation ("IRR") ensemble, the reconstructions of areas historically equipped for irrigation were used, while in the control ("CTL") ensemble, irrigated area was set to zero.

We selected eight initial conditions from a 6,000-year pre-industrial ESM2Mb run, which was an extended version of an experiment already documented (Dunne et al., 2012, 2013); we initialized our experiments from years 0001, 5300, 5400, 5500, 5600, 5700, 5800, and 5900. For spin-up, starting from each of the eight initial conditions, we conducted historical simulations without irrigation from 1850 through 1901. Starting from the end states of those eight simulations, we ran an ensemble of eight IRR experiments (historical forcing, including irrigation) and an ensemble of eight CTL experiments (historical forcing, but without irrigation) for 1902 through 2015. The historical forcing included both anthropogenic forcing (i.e., atmospheric greenhouse gas and aerosol concentrations and land-use transitions) and natural forcing (i.e., solar irradiance and atmospheric aerosols from volcanoes), which were prescribed on the basis of estimated historical and "RCP4.5" data, following the experimental design for the Coupled Model Intercomparison Project, Phase 5 (Taylor et al., 2012). In IRR, the irrigated area in each grid cell changed annually from 1902 through 2015 based on a historical data set (Hurtt et al., 2020). Results presented in the paper are ensemble means.

3. Results

The accelerating growth of global irrigated area from 0.5 to 3.0 million km^2 during 1902–2015 (Hurtt et al., 2020) drives similar growth of the annual amount of water application for irrigation in the model (Figure S1a in Supporting Information S1). Over the period 1902–2015, the global annual irrigation amount averages about 540 km^3, with annual irrigation depth (volume of water added per unit of irrigated area) of 300 mm, reaching about 1,110 km^3 (310 mm) by 2015; for comparison, modeled global annual land precipitation (P) is 128,000 km^3 (850 mm over entire land area).

To assess the suitability of the model for investigation of irrigation impacts, we first compared modeled irrigation amounts to the amounts calculated independently for 10 major regions of the world, for the year 2010, in a comprehensive synthesis of statistics on climate, water-balance, and crop water-requirements (Frenken & Gillet, 2012). Irrigation amount biases (Figure S1b in Supporting Information S1) are related to precipitation biases (in North America, Western Europe, and East Asia) and to the omission of flood irrigation (in South and Southeast Asia) in the model, neither of which is likely to affect our findings. With approximate adjustments for these biases (see Text S2 in Supporting Information S1), regional estimates of irrigation amounts from ESM2Mb explained 90% of the variance of irrigation amount across the regions, and the global irrigation amount of 1,430 km^3 y^{-1} compared favorably with the independent estimate of 1,500 km^3 y^{-1}.

On average over 1986–2015, irrigation enhances evapotranspiration (E) on the irrigated fractions of land grid cells by an amount (1,070 km^3 y^{-1}) approximately equal to the irrigation amount (1,030 km^3 y^{-1}) and on land outside irrigated areas by an additional 1,000 km^3 y^{-1}, while precipitation increases by 1,590 km^3 y^{-1} (1.2%) over land. The 480-km^3 y^{-1} net reduction of land P-E is balanced by an equal reduction in net flux of moisture from ocean to atmosphere.

Most of the regions of the largest statistically significant IRR-CTL differences in precipitation (P) are adjacent to or collocated with extensive areas of large-scale irrigation (Figure 1). These regions include South Asia, the eastern high mountain ranges of Asia (Pamir, Hindu Kush, Karakoram, Kunlun Shan, western Himalaya), and the Armenian Highlands.

The model's response to irrigation is weak in North America, Europe, and northeastern China. This weak response can be understood as a result of the positive bias in precipitation in those regions, which suppress irrigation, as already mentioned, but these regional biases are not expected to affect the model's representation of response to irrigation in Africa.

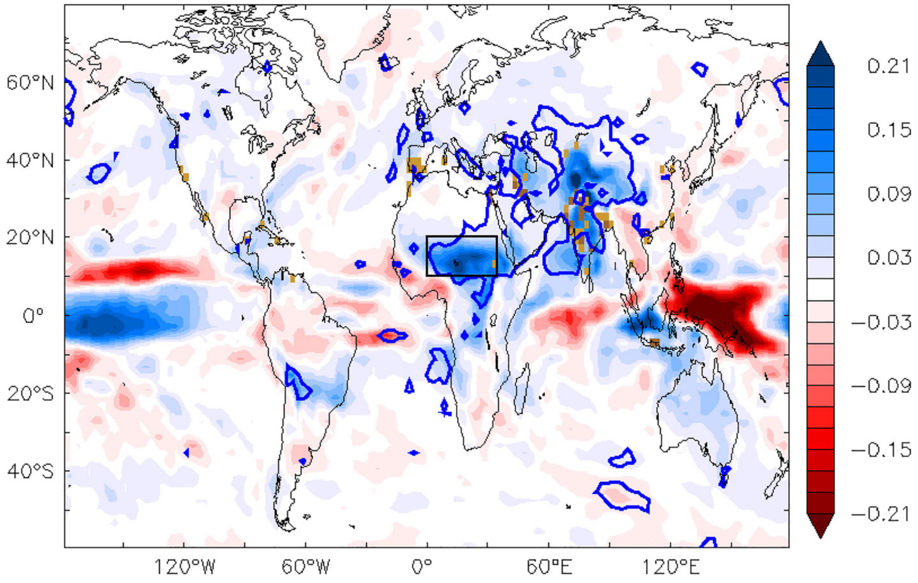

Figure 1. Modeled global distribution of precipitation difference (mm d^{-1}) resulting from irrigation, 1902–2015. Model grid cells having annual, cell-average irrigation amounts lower than 150 mm and greater than 50 mm are colored light brown; cells with amounts greater than 150 mm are colored dark brown. Blue contours enclose the areas where the magnitude of the *t* statistic for the ensemble-average of the difference between the eight paired irrigated (IRR) and control (CTL) experiments is greater than 3. Black box (0°–35°E, 10°–20°N) indicates the focus region of this study.

The only remote region of large *P* response is located in northern tropical Africa; in the analyses that follow, we focus on a geographic region (0°–35°E, 10°–20°N) of relative maximum of *P* response combined with a high value (>3) of the *t* statistic (Figure 1). (Although formal conditions for application of Student's *t* test are not met here, because the grid cells are not independent, the scarcity of *t* values greater than 3 in regions far from large-scale irrigation confirms that our criterion is conservative.) For time averages, we use data for the 30-year period 1986–2015, when irrigation was the highest, unless otherwise noted.

The average annual precipitation over the analysis region is 790 (830) mm in CTL (IRR), with a pronounced wet season during boreal summer (Figure 2a) and a strong meridional gradient. This spatio-temporal structure of the model's precipitation is very similar to observations from the Global Precipitation Climatology Centre (GPCC; Global Precipitation Climatology Centre, 2018), with the model explaining 83% of the shape of the annual cycle and 85% of the spatial distribution, thus reproducing the imprint of the West African monsoon. This agreement for the annual cycle is expected, because climate models often capture the overall shape of the annual cycle in precipitation, with a single seasonal maximum north of 10°N (Dunning et al., 2017).

Despite qualitative agreement, the GPCC data show that the actual annual precipitation over the SSS region (averaging 340 mm) is much lower than in the model, indicating a bias that has also been noted by a previous study (Monerie et al., 2017). The model's Köppen-Geiger climate zones (Beck et al., 2018) in the SSS box are differentiated mainly by annual precipitation, and they range from hot, arid desert (BWh; 33% and 28% of area in CTL and IRR, respectively) in the north, through hot, semi-arid steppe (BSh; 23%, 24%), to tropical savanna with dry winter (Aw; 44%, 48%) in the south. In contrast, observations yield 66% area BWh, 27% BSh, and 7% Aw. The biases in the distribution of climate types is explained mainly by a northward bias of the extent of monsoon precipitation in the model.

We account for the bias in our model climate in two ways. (a) We used the relative (i.e., percentage), rather than absolute, change of precipitation as a measure of sensitivity. (b) We interpret our results as indicative of potential sensitivity of precipitation in a region that is actually centered somewhat south of the model's study region. If the box defining the study region is shifted southward by 4° latitude (i.e., 6°–16°N, 0–35°E), the annual cycle of GPCC precipitation, with an average value of 800 mm, is very similar to that of the model at 10°–20°N (Figure 2a), and, accordingly, the areas of climate types are similar to those in the model in the study area (26%

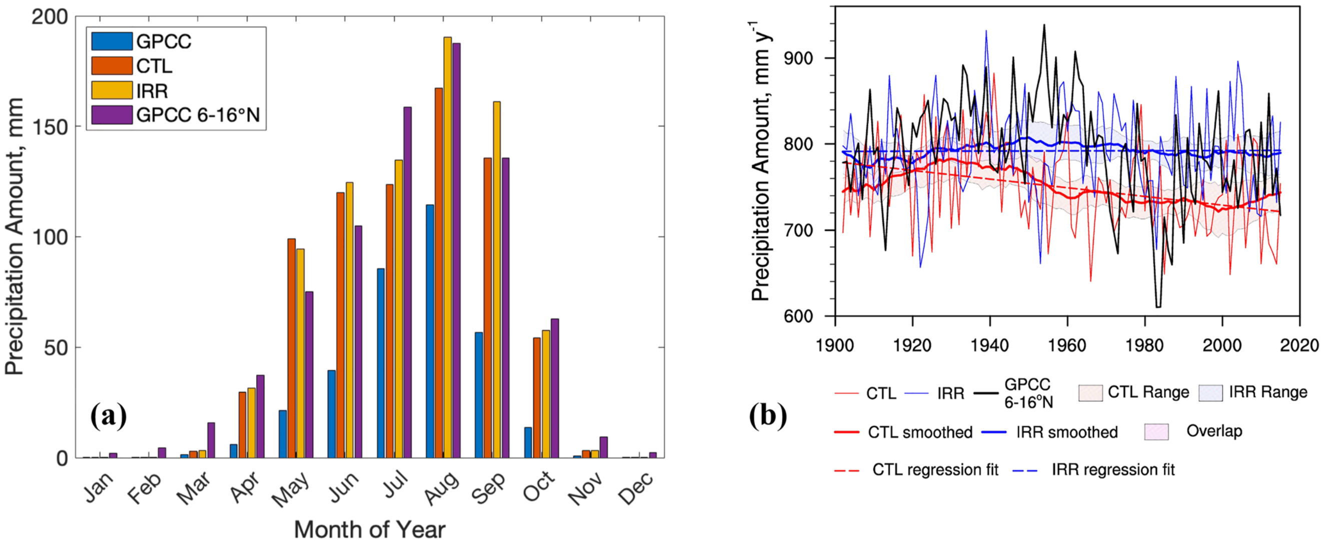

Figure 2. Seasonal cycle and annual time series of precipitation averaged over the Sahel-Sudan Savanna region. (a) Seasonal cycle of precipitation in Global Precipitation Climatology Centre (GPCC; Global Precipitation Climatology Centre, 2018) observations (for the study region and for a southward shift of the study region) and in control (CTL) and irrigated (IRR) ensembles, averaged over 1986–2015. (b) Annual time series and smoothed (30-year moving average) time series of precipitation in GPCC observations (for a southward shift of the study region) and in CTL and IRR. Shaded ranges represent smoothed values plus and minus twice the standard error of estimation of the ensemble mean.

BWh, 28% BSh, 46% Aw). With or without the southward displacement, our study region is contained mostly by the SSS (Sayre et al., 2013; SSS), and we shall use that designation henceforth.

The 8.5% difference (IRR-CTL) in annual precipitation is concentrated disproportionately in July through September ("JAS"), at the height of the West African monsoon rain season (Figure 2a); the difference during JAS alone is 14%. In the CTL ensemble, annual precipitation in the SSS trends downward at a rate of −6% per century over the 1902–2015 period (Figure 2b). A forced downward precipitation trend in the SSS is consistent with earlier findings obtained using the physical climate model (i.e., CM2.1) upon which ESM2Mb was built (Held et al., 2005). In IRR, the ensemble trend (+0.1% per century) is almost absent. Consistent with the high significance of the ensemble precipitation difference in the study region, the time series of CTL and IRR, although overlapping in the early 1900s, clearly separate during the later decades.

The downward trend in the CTL ensemble is consistent with observations; we find a GPCC trend of −6% per century for the study region (−10% for the 4°-southward-shifted region). Although the ensemble-average difference between IRR and CTL is significant, the eight CTL ensemble members have trends ranging from −19 to +9% per century, and the eight IRR ensemble members have trends ranging from −8 to +5% per century. Thus, because of the strength of internal variability, and given the uncertainty in climate forcing, the difference between the IRR and CTL trends cannot be readily distinguished by the observational record.

By what mechanism(s) does remote, large-scale irrigation drive an increase of SSS precipitation in our model? In view of the enhancement of atmospheric humidity by irrigation, an increased supply of atmospheric moisture downwind of irrigated areas has been advanced as an explanation for remote precipitation increases (de Vrese et al., 2016). In our experiments, however, we find that the moisture flux entering the SSS region across its northern and eastern borders is actually reduced by irrigation (from 3,020 to 2,780 $\text{km}^3\ \text{y}^{-1}$ averaged over 1986–2015), due to a slowing of the winds that more than offsets the increased humidity. It can be concluded that an enhanced northeasterly inflow of water vapor from irrigation is not the driver of the precipitation increase in these experiments.

The spatial and temporal distributions and variability of precipitation in West Africa are the result of the interaction of multiple complex dynamical processes and features, including the Hadley circulation, the Inter-Tropical Convergence Zone, the West African monsoon, the African Easterly Jet, and interactions of the atmosphere with vegetation, albedo, and soil moisture on land (Biasutti, 2019; Charney, 1975; K. H. Cook, 1999). Despite this complexity, insights into the sensitivity of the prevailing large-scale precipitation pattern to forced perturbations of the atmosphere can be obtained by considering the budget of vertically integrated MSE (Hill et al., 2017).

The modification of the MSE budget originates over the irrigated region. During the JAS season in the model, the evapotranspiration increase induced by irrigation (Text S3 and Figure S2 in Supporting Information S1) feeds a plume of atmospheric moistening in the vicinity and generally downwind of the irrigated regions of the Tigris-Euphrates, Nile, and Indus River valleys (Figure 3a). The MSE also increases in this area (Figure 3b); this increase is attributable to the increased top-of-atmosphere (TOA) radiative heating of the land-atmosphere system in the irrigated region (Figure 3c), which partially compensates for the direct cooling influence of irrigation. The radiation change is mainly a result of a decrease in TOA outgoing longwave radiation, which is driven by both the moistening (which raises the effective longwave emission level) and the cooling (which decreases the upward longwave radiation from any given level) of the atmosphere.

In both CTL and IRR, the MSE of air in the Sahara Desert is less than that south of the SSS, because the contribution from the higher temperature of Saharan air is more than offset by the contribution from the higher humidity to the south. As a consequence of the horizontal MSE gradient, the air carried by the northerly winds must consume energy to raise its MSE from that of the Sahara to that south of the SSS (Hill et al., 2017). Because remote irrigation in IRR increases the MSE of the northerly air flow, the energy consumed to raise the MSE of the northerly air flow decreases by 3.6 W m^{-2} in IRR compared with CTL. This change must be offset by adjustments to other terms in the MSE budget. It is partially balanced by a 0.2 W m^{-2} decrease in TOA radiation and a 1.5 W m^{-2} increase in the combined term of divergence of horizontal MSE eddy fluxes and MSE transient storage. The change in vertical advection absorbs the remaining 1.9 W m^{-2} and is associated with an increase in upward motion (Figure 3d), which drives the increase in precipitation (Figure 3e; see Text S4 in Supporting Information S1 for a more formal description of the MSE budget and the hydroclimatic consequences of its perturbation by remote irrigation).

4. Discussion and Conclusions

4.1. Biases, Uncertainties, and Sensitivities

Here we assess uncertainties in our study resulting from sensitivities to biases in the model dynamics and our modeling assumptions. The causal chain in our study consists of (a) irrigation over irrigated area and its local impacts on evapotranspiration and MSE in the Middle East and South Asia, (b) MSE transport to North Africa by the prevailing circulation, (c) MSE advection conversion (from horizontal to vertical term) in the SSS region, (d) enhancement of upward motion and precipitation in the SSS region. To exam the uncertainties involved in each link of the chain, some analyses against observations and/or previous research were performed.

For (a), the estimate of irrigation amount (as well as irrigation-induced evapotranspiration) will be positively biased by assumption that plant water requirements are fully satisfied. On the other hand, the overall effect of neglecting irrigation conveyance losses will be to underestimate the impact of irrigation on the atmosphere, because some fraction of the water lost in conveyance would enhance evapotranspiration. Furthermore, continuous irrigation will minimize seepage losses (drainage from the root zone) and therefore require application of less water to satisfy plant water needs. Most importantly, however, our evaluation of the simulated irrigation amounts in Section 2 and Text S2 in Supporting Information S1 showed that those amounts compared favorably with independent estimates after approximate adjustments for precipitation and flood irrigation biases.

For (b), we evaluated the simulated atmospheric circulation pattern that links the irrigated regions and the SSS by comparing the JAS vapor transport in ESM2Mb to the European Centre for Medium-Range Weather Forecasts “ERA5” reanalysis (Hersbach et al., 2020; Text S5 in Supporting Information S1). We found that the vapor transport fields were qualitatively similar, but also that quantitative deficiencies in the model's circulation pattern may cause the model to overestimate the influence of remote irrigation on SSS precipitation.

For (c), we defiend a term called “advection conversion efficiency” which is the ratio of the increase in vertical advection of MSE to the reduction in horizontal advection, and compared the advection conversion efficiency for the 16 model experiments and three recent-generation atmospheric reanalysis products (Text S6 in Supporting Information S1). The results show that the distribution of efficiencies estimated from our experiments are consistent with the values from the reanalysis datasets, indicating that in ESM2Mb transformation of the horizontal

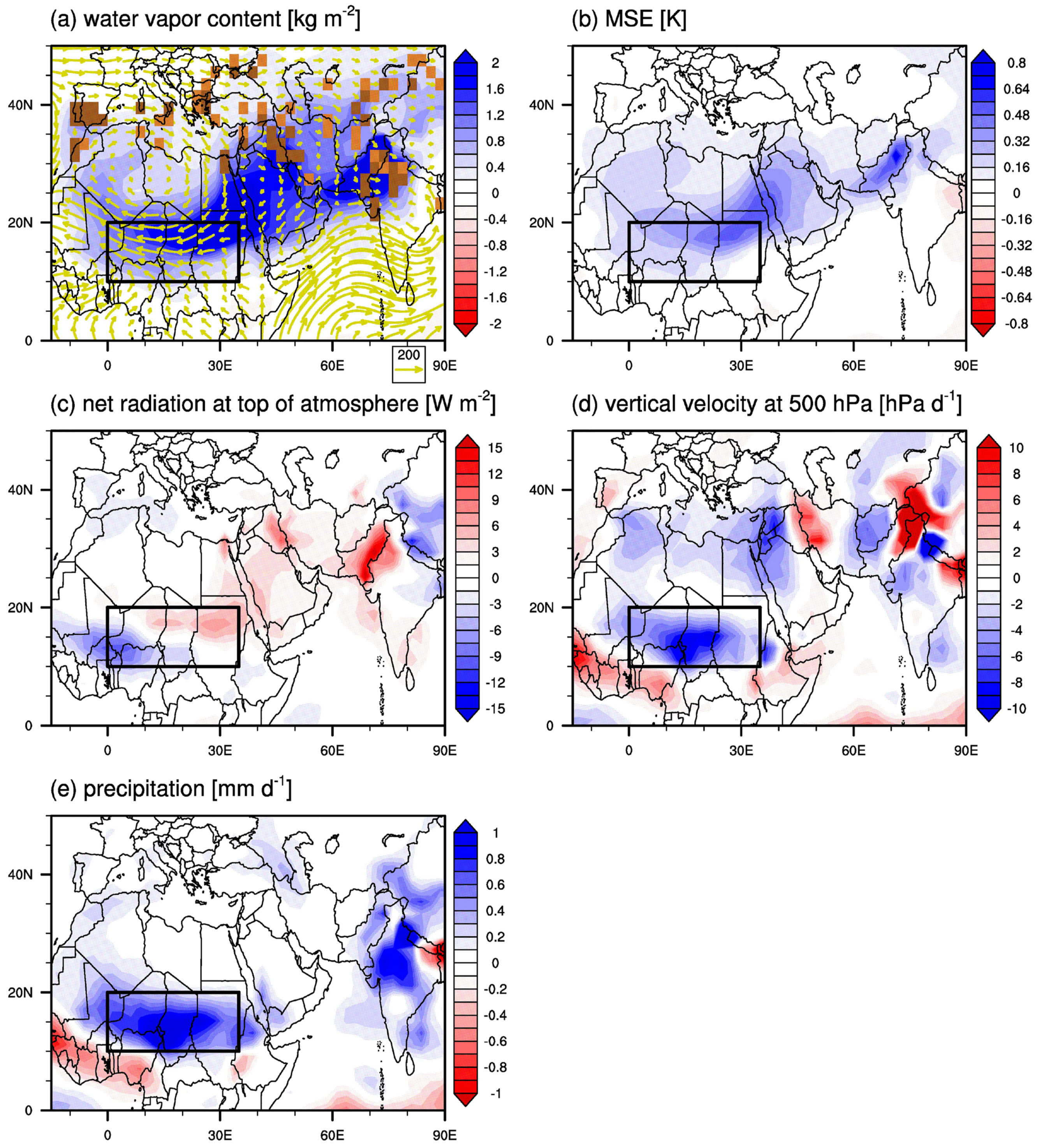

Figure 3. Differences (IRR-CTL) of atmospheric humidity, moist static energy (MSE), radiative heating, vertical velocity, precipitation during JAS, 1986–2015. (a) Vertically integrated water-vapor content, kg m^{-2}. Arrows indicate horizontal flux of water vapor, vertically integrated over full atmospheric column, in CTL, kg m^{-1} s^{-1}. Model grid cells having annual, cell-average irrigation amounts lower than 150 mm and greater than 50 mm are colored light brown; cells with amounts greater than 150 mm are colored dark brown. (b) MSE divided by specific heat of air at constant pressure, c_p, and averaged between 700 hPa and surface, K. (c) Net radiation at top of atmosphere, positive downward, W m^{-2}. (d) Pressure-coordinate vertical velocity ("omega") at 500 hPa level, hPa d^{-1}. (e) Precipitation, mm d^{-1}.

advection of MSE to vertical advection in the SSS is within the observationally based range and supports the conclusion of our MSE budget analysis of the mechanisms controlling remote impact of irrigation.

Besides the MSE horizontal and vertical advection terms, precipitation-radiation feedback also plays a role in the MSE budget, as shown by the right side of the Equation S2 in Supporting Information S1. We assessed the sensitivity of radiation to precipitation in the context of our experiment by comparing the modeled and observed (Harris et al., 2020; Kato et al., 2018; Loeb et al., 2018) relations between the annual time series of JAS TOA net radiation and precipitation, with consideration of their spatial variation over the SSS region. We infer from the comparison (Text S7 in Supporting Information S1) that ESM2Mb's radiation response to the IRR-CTL increase in precipitation is biased low. The direct response to correction of this bias in the MSE budget would lead to further increase of vertical advection and precipitation, thereby amplifying the precipitation enhancement in the SSS.

For (d), in a previous analysis of the sensitivity of ESM2Mb's atmospheric component to mean ocean-surface cooling (Hill et al., 2017; which produces an increase of West African precipitation that is somewhat analogous to the effect of irrigation), the precipitation over a study region very similar to ours reached a maximum that could not be exceeded, regardless of the amount of further ocean cooling. Our CTL experiment's wet bias places it already near that upper limit of precipitation, even without irrigation. It is therefore conceivable that this wet bias limits the amount that precipitation can increase, implying that our estimate of precipitation sensitivity to irrigation could be conservative.

4.2. Model-Dependence of Results

Model-based results, such as those described here, are model-dependent, and every model is imperfect in its own way. The plausibility of model-based findings can be strengthened by inter-model agreement, by mechanistic elucidation of the processes underlying those findings, and by evaluation of the biases in those processes and the sensitivity of results thereto. Other models that have shown precipitation enhancement (or resultant latent heat flux increase) in the SSS region are the NASA GISS model (Puma & Cook, 2010, Figure 6; B. I. Cook et al., 2015, Figure 8) and the NCAR CESM 1.2 model (Thiery et al., 2017, Figure 4; Zeng et al., 2017, Figure 6), while the Max Planck Institute model ECHAM6 produced an enhancement of precipitation only in Eastern Africa (de Vrese et al., 2016, Figure 1). In contrast to these earlier studies, and in view of the differences in their responses, our study elucidated the mechanistic underpinnings of the modeled response, following the multi-step causal chain from irrigation to SSS precipitation and evaluating the sensitivities of the analysis to biases by use of a variety of relevant observations.

We suggest that a model intercomparison based on a common experimental design (B. I. Cook et al., 2015; Thiery et al., 2017) and adopting the mechanistic approach taken here, might reduce uncertainty in the magnitude of the SSS precipitation response to remote irrigation. Model climatologies of circulation, MSE dynamics, radiation, and convection (Hill et al., 2017, 2018) need to be assessed, as do inter-model differences in irrigation parameterizations, crop schedules and model precipitation amounts, all of which affect irrigation amounts and resultant evapotranspiration changes.

4.3. Relevance to Water Security

Our findings have implications for interpretation of the historical climate record and for assessment of possible futures. The irrigation signal estimated by our model is unlikely to be detectable above internal variability and forced variations, but its magnitude is not negligible in societal or ecological terms and would be sufficient to affect risks of drought and famine. In the two driest years of the SSS drought of the 1970s and 1980s, which was driven largely by anomalous ocean-surface temperatures (Biasutti, 2019; Giannini et al., 2003; Held et al., 2005), the annual precipitation, averaged over the SSS study region, was 26% (in 1973) and 42% (in 1984) below the 1902–2015 mean. Over the driest 20-year period (1971–1990), precipitation averaged 14% below the mean. For the same period, the modeled enhancement of precipitation by irrigation was 7%.

Future growth of global irrigation is uncertain. Projection of recent trends suggests only modest growth (Alexandratos & Bruinsma, 2012), although some socioeconomic scenarios would entail much more rapid growth (Hurtt et al., 2020). On a regional scale, trends will depend on regionally unique socioeconomic and geopolitical factors.

Future changes of water availability in the SSS may be tied not only to internal climate variability and greenhouse gas and aerosol emissions, but also to the factors that will affect the amount of future remote irrigation. These include the potential exhaustion of non-renewable groundwater resources in South Asia (Rodell et al., 2009; Zeng et al., 2017), which are presently used for irrigation, and the rehabilitation of irrigation infrastructure in the Tigris-Euphrates valley that was damaged or destroyed during the political conflict of the mid 2010s (Food and Agricultural Organization of the United Nations, 2018).

Data Availability Statement

The ESM2M model is available at https://mom-ocean.github.io. ESM2Mb can be obtained from ESM2M by specifying values of a small number of parameters, as follows: In river_physics_nml: prohibit_cold_ice_outflow=.FALSE.; in vegn_data_nml: cnst_crit_phen(0:4) = 0.30, 0.15, 0.15, 0.30, 0.30; alpha(0:4,6) = 0.0, 0.0, 0.012, 0.012, 0.012; treefall_disturbance_rate = 0.175, 0.185, 0.025, 0.0275, 0.027. The GPCC precipitation data can be obtained from https://psl.noaa.gov/data/gridded/data.gpcc.html. The recorded FAO irrigation amount data can be obtained from https://www.fao.org/aquastat/en/databases. The ERA5 reanalysis data can be obtained from https://cds.climate.copernicus.eu/cdsapp#!/dataset/reanalysis-era5-pressure-levels-monthly-means?tab=form. The MERRA and MERRA2 reanalysis data can be obtained from https://gmao.gsfc.nasa.gov/reanalysis.

Acknowledgments
The authors gratefully acknowledge critiques of early drafts of this work by Tom Delworth, Nathalie de Noblet-Ducoudré, John Dunne, Tom Knutson, Isaac Held, and anonymous reviewers. Y. Zeng received financial support under award NA18OAR4320123 from the National Oceanic and Atmospheric Administration (NOAA), U.S. Department of Commerce, through the Cooperative Institute for Modeling the Earth System (CIMES) at Princeton University. M. H. J. van Huijgevoort and Y. Zeng received financial support from the High Meadows Environmental Institute's Carbon Mitigation Initiative at Princeton University, and from the NOAA-funded Cooperative Institute for Climate Science (CICS) at Princeton University, a predecessor of CIMES. Any statements, findings, conclusions, or recommendations of this report are those of the authors and do not necessarily reflect the views of the NOAA or the U.S. Department of Commerce.

References

Alexandratos, N., & Bruinsma, J. (2012). World agriculture towards 2030/2050: The 2012 revision. *ESA Working Paper No. 12-03* (p. 147). Food and Agriculture Organization of the United Nations, Agricultural Development Economics Division.

Back, L. E., & Bretherton, C. S. (2006). Geographic variability in the export of moist static energy and vertical motion profiles in the tropical Pacific. *Geophysical Research Letters*, *33*(17). https://doi.org/10.1029/2006gl026672

Beck, H. E., Zimmermann, N. E., McVicar, T. R., Vergopolan, N., Berg, A., & Wood, E. F. (2018). Present and future Köppen-Geiger climate classification maps at 1-km resolution. *Scientific Data*, *5*, 180214. https://doi.org/10.1038/sdata.2018.214

Biasutti, M. (2019). Rainfall trends in the African Sahel: Characteristics, processes, and causes. *Wiley Interdisciplinary Reviews: Climate Change*, *10*, e59. https://doi.org/10.1002/wcc.591

Charney, J. G. (1975). Dynamics of deserts and drought in the Sahel. *Quarterly Journal of the Royal Meteorological Society*, *101*(428), 193–202. https://doi.org/10.1002/qj.49710142802

Cook, B. I., Shukla, S. P., Puma, M. J., & Nazarenko, L. S. (2015). Irrigation as an historical climate forcing. *Climate Dynamics*, *44*, 1715–1730. https://doi.org/10.1007/s00382-014-2204-7

Cook, K. H. (1999). Generation of the African easterly jet and its role in determining West African precipitation. *Journal of Climate*, *12*, 1165–1184. https://doi.org/10.1175/1520-0442(1999)012<1165:gotaej>2.0.co;2

de Vrese, P., Hagemann, S., & Claussen, M. (2016). Asian irrigation, African rain: Remote impacts of irrigation. *Geophysical Research Letters*, *43*, 3737–3745. https://doi.org/10.1002/2016gl068146

Dunne, J. P., John, J. G., Adcroft, A. J., Griffies, S. M., Hallberg, R. W., Shevliakova, E., et al. (2012). GFDL's ESM2 global coupled climate-carbon Earth system models. Part I: Physical formulation and baseline simulation characteristics. *Journal of Climate*, *25*, 6646–6665. https://doi.org/10.1175/jcli-d-11-00560.1

Dunne, J. P., John, J. G., Shevliakova, E., Stouffer, R. J., Krasting, J. P., Malyshev, S. L., et al. (2013). GFDL's ESM2 global coupled climate-carbon Earth system models. Part II: Carbon system formulation and baseline simulation characteristics. *Journal of Climate*, *26*, 2247–2267. https://doi.org/10.1175/jcli-d-12-00150.1

Dunning, C. M., Allan, R. P., & Black, E. (2017). Identification of deficiencies in seasonal rainfall simulated by CMIP5 climate models. *Environmental Research Letters*, *12*, 114001. https://doi.org/10.1088/1748-9326/aa869e

Food and Agricultural Organization of the United Nations. (2018). *Iraq: Restoration of agriculture and water systems sub-programme 2018–2020* (p. 110). Licence CC BY-NC-SA 3.0 IGO.

Frenken, K., & Gillet, V. (2012). Irrigation water requirement and water withdrawal by country. *Food and Agriculture Organization of the United Nations AQUASTAT Report* (p. 263).

Giannini, A., Saravanan, R., & Chang, P. (2003). Oceanic forcing of Sahel rainfall on interannual to interdecadal time scales. *Science*, *302*(5647), 1027–1030. https://doi.org/10.1126/science.1089357

Global Precipitation Climatology Centre. (2018). *GPCC full data monthly product version 2018, precipitation in mm/month, 0.5 degree*. Deutsche Wetterdienst.

Guimberteau, M., Laval, K., Perrier, A., & Polcher, J. (2013). Global effect of irrigation and its impact on the onset of the Indian summer monsoon. *Climate Dynamics*, *39*, 1329–1348. https://doi.org/10.1007/s00382-011-1252-5

Harris, I., Osborn, T. J., Jones, P., & Lister, D. (2020). Version 4 of the CRU TS monthly high-resolution gridded multivariate climate dataset. *Scientific Data*, *7*(1), 1–18. https://doi.org/10.1038/s41597-020-0453-3

Held, I. M., Delworth, T. L., Lu, J., Findell, K. L., & Knutson, T. R. (2005). Simulation of Sahel drought in the 20th and 21st centuries. *Proceedings of the National Academy of Sciences*, *102*, 17891–17896. https://doi.org/10.1073/pnas.0509057102

Hersbach, H., Bell, B., Berrisford, P., Hirahara, S., Horányi, A., Muñoz-Sabater, J., et al. (2020). The ERA5 global reanalysis. *Quarterly Journal of the Royal Meteorological Society*, *146*, 1999–2049. https://doi.org/10.1002/qj.3803

Hill, S. A., Ming, Y., Held, I. M., & Zhao, M. (2017). A moist static energy budget-based analysis of the Sahel rainfall response to uniform oceanic warming. *Journal of Climate*, *30*, 5637–5660. https://doi.org/10.1175/jcli-d-16-0785.1

Hill, S. A., Ming, Y., & Zhao, M. (2018). Robust responses of the Sahelian hydrological cycle to global warming. *Journal of Climate*, *31*, 9793–9814. https://doi.org/10.1175/jcli-d-18-0238.1

Hurtt, G. C., Chini, L., Sahajpal, R., Frolking, S., Bodirsky, B. L., Calvin, K., et al. (2020). Harmonization of global land-use change and management for the period 850–2100 (LUH2) for CMIP6. *Geoscientific Model Development Discussions*, *13*, 5425–5464. https://doi.org/10.5194/gmd-13-5425-2020

Inoue, K., & Back, L. (2015). Column-integrated moist static energy budget analysis on various time scales during TOGA COARE. *Journal of the Atmospheric Sciences*, *72*(5), 1856–1871. https://doi.org/10.1175/jas-d-14-0249.1

Jalihal, C., Srinivasan, J., & Chakraborty, A. (2020). Different precipitation response over land and ocean to orbital and greenhouse gas forcing. *Scientific Reports*, *10*, 11891. https://doi.org/10.1038/s41598-020-68346-y

Kato, S., Rose, F. G., Rutan, D. A., Thorsen, T. J., Loeb, N. G., Doelling, D. R., et al. (2018). Surface irradiances of edition 4.0 Clouds and the Earth's Radiant Energy System (CERES) Energy Balanced and Filled (EBAF) data product. *Journal of Climate*, *31*(11), 4501–4527. https://doi.org/10.1175/jcli-d-17-0523.1

Loeb, N. G., Doelling, D. R., Wang, H., Su, W., Nguyen, C., Corbett, J. G., et al. (2018). Clouds and the Earth's radiant energy system (CERES) energy balanced and filled (EBAF) top-of-atmosphere (TOA) edition-4.0 data product. *Journal of Climate*, *31*(2), 895–918. https://doi.org/10.1175/jcli-d-17-0208.1

Malyshev, S., Shevliakova, E., Stouffer, R. J., & Pacala, S. W. (2015). Contrasting local versus regional effects of land-use-change-induced heterogeneity on historical climate: Analysis with the GFDL Earth system model. *Journal of Climate*, *28*, 5448–5469. https://doi.org/10.1175/jcli-d-14-00586.1

Masunaga, H. (2012). Short-term versus climatological relationship between precipitation and tropospheric humidity. *Journal of Climate*, *25*, 7983–7990. https://doi.org/10.1175/jcli-d-12-00037.1

Milly, P. C. D., Malyshev, S. L., Shevliakova, E., Dunne, K. A., Findell, K. L., Gleeson, T., et al. (2014). An enhanced model of land water and energy for global hydrologic and Earth-system studies. *Journal of Hydrometeorology*, *15*, 1739–1761. https://doi.org/10.1175/jhm-d-13-0162.1

Monerie, PA., Sanchez-Gomez, E., & Boé, J. (2017). On the range of future Sahel precipitation projections and the selection of a sub-sample of CMIP5 models for impact studies. *Climate Dynamics*, *48*, 2751–2770. https://doi.org/10.1007/s00382-016-3236-y

Puma, M. J., & Cook, B. I. (2010). Effects of irrigation on global climate during the 20th century. *Journal of Geophysical Research*, *115*, D16120. https://doi.org/10.1029/2010jd014122

Raymond, D. J. (2000). Thermodynamic control of tropical rainfall. *Quarterly Journal of the Royal Meteorological Society*, *126*, 889–898. https://doi.org/10.1002/qj.49712656406

Rodell, M., Velicogna, I., & Famiglietti, J. S. (2009). Satellite-based estimates of groundwater depletion in India. *Nature*, *460*, 999–1002. https://doi.org/10.1038/nature08238

Sayre, R., Comer, P., Hak, J., Josse, C., Bow, J., Warner, H., et al. (2013). *A new map of standardized terrestrial ecosystems of Africa* (p. 24). Association of American Geographers.

Shevliakova, E., Pacala, S. W., Malyshev, S., Hurtt, G. C., Milly, P. C. D., Caspersen, J. P., et al. (2009). Carbon cycling under 300 years of land use change: Importance of the secondary vegetation sink. *Global Biogeochemical Cycles*, *23*, GB2022. https://doi.org/10.1029/2007GB003176

Taylor, K. E., Stouffer, R. J., & Meehl, G. A. (2012). An overview of CMIP5 and the experiment design. *Bulletin of the American Meteorological Society*, *93*, 485–498. https://doi.org/10.1175/bams-d-11-00094.1

Thiery, W., Davin, E. L., Lawrence, D. M., Hirsch, A. L., Hauser, M., & Seneviratne, S. I. (2017). Present-day irrigation mitigates heat extremes. *Journal of Geophysical Research: Atmospheres*, *122*, 1402–1422. https://doi.org/10.1002/2016jd025740

Wei, J., Dirmeyer, P. A., Wisser, D., Bosilovich, M. G., & Mocko, D. M. (2013). Where does the irrigation water go? An estimate of the contribution of irrigation to precipitation using MERRA. *Journal of Hydrometeorology*, *14*, 275–289. https://doi.org/10.1175/jhm-d-12-079.1

Zeng, Y., Xie, Z., & Zou, J. (2017). Hydrologic and climatic responses to global anthropogenic groundwater extraction. *Journal of Climate*, *30*, 71–90. https://doi.org/10.1175/jcli-d-16-0209.1

References From the Supporting Information

Gelaro, R., McCarty, W., Suárez, M. J., Todling, R., Molod, A., Takacs, L., et al. (2017). The modern-era retrospective analysis for research and applications. *Journal of Climate*, *30*, 5419–5454. https://doi.org/10.1175/jcli-d-16-0758.1

Rienecker, M., Suarez, M. J., Gelaro, R., Todling, R., Bacmeister, J., Liu, E., et al. (2011). MERRA: NASA's modern-era retrospective analysis for research and applications. *Journal of Climate*, *24*, 3624–3648. https://doi.org/10.1175/jcli-d-11-00015.1